Computational study of fluid flow in tapered orifices for needle-free injectors

Yatish S. Rane, Jeremy O. Marston*

Department of Chemical Engineering, Texas Tech University, Lubbock, TX 79409, USA

ABSTRACT

Transdermal drug delivery using spring-powered jet injection has been studied for several decades and continues to be highly sought after due to the advent of targeted needle-free techniques, especially for viscous and complex fluids. As such, this paper reports results from numerical simulations to study the role of fluid rheology and cartridge geometry on characteristics such as jet exit velocity, total pressure drop and boundary layer thickness, since these all factor in to jet stability and collimation. The numerical approach involves incompressible steady flow with turbulence modelling based on the system Reynolds number at the orifice ($Re = \rho d_o v_j / \mu$). The results are experimentally validated for a given geometry over a wide range of Reynolds numbers ($10^1 < Re < 10^4$), and our results indicate a sharp decrease in dimensionless pressure drop ($Eu = 2\Delta P / \rho v_j^2$) for $Re < 10^{2)}$ and gradually approaching the inviscid limit at $Re \geq 10^4$. By extending the study to non-Newtonian fluids, whose rheological profile is approximated by the Carreau model, we also elucidated the effect of different rheological parameters. Lastly by studying a range of nozzle geometries such as conical, sigmoid taper and multi-tier tapers, we observe that fluid acceleration suppresses the boundary layer growth, which indicates there may be optimal geometries for creating jets to target specific tissue depths.

1. Introduction

Needle-free jet injectors produce high-speed liquid jets which can deliver drugs across the skin and deposit at different depths inside the body, depending on jet characteristics. The concept of needle-free jet injection has been reported in the clinical setting since the 1940's [1] and has therefore been studied for more than half a century, with more intense interest in the last two decades in understanding physics of jet injections [2–4]. Needle-free jet injection has the flexibility to deliver drugs into intramuscular region (inside the muscle), subcutaneous region (fat layer underneath the skin), and potentially intradermal region (into the epidermis and dermis, immediately below the stratus cornea), shown in Fig. 1. There can be various actuation sources for generating high speed liquid jets, such as spring force [5–8], compressed gas [9], Lorentz actuators [10], voice coil [11], and pulsed lasers [12]. Due to the simple mechanism and low-cost of manufacturing, spring-powered needle-free jet injection devices have an enormous potential in mass immunizations, especially in the developing world. Jet injections can also resolve needle-phobia [13] (trypanophobia) along with crucial issues such as needle stick injuries [3]. Although there are many advantages of jet injections, there is reluctance toward using these devices in medical professionals along with patients due to the high costs, inconsistency [14], occasional bruising and pain [13].

The intradermal region refers to the epidermis and dermis, located beneath the outer layer of the skin, which constitutes the first layer of protection from the outside environment [15] and is host to a variety of immune cells [15–17]. For this reason, intradermal drug delivery can augment immune response and facilitate fractional dose vaccination [18,19]. Intradermal injections may potentially reduce the occurrence and intensity of pain associated with injection due to the low presence of pain sensory nerves [15]. However, the total thickness of the dermal tissue is approximately 4 mm and so, the limit of allowed variation in target depths for jet injection is very small [20], and very few devices have been specifically designed for delivering intradermal injections [21–23].

Another factor dictating the increased interest in jet injection is the advent of DNA-based vaccines, which are seen as promising biological drugs [16,24], but may need to be delivered in high concentration to increase potency [16]. This can render fluids that are both high-viscosity and non-Newtonian (shear-thinning), which creates challenges relating to injectability [25,26].

The basic premise behind jet injectors is that a high upstream pressure in the drug cartridge (ampoule) forces liquid from an orifice at high speed, yet the role of geometry, where the cartridge tapers toward the orifice has not yet been fully studied. This is especially relevant in the context of non-Newtonian fluids, such as DNA vaccines. Commercially feasible needle-free jet injectors need to be consistent with regards to efficient drug delivery and ability to reach target injection depths reliably for a range of rheological properties [27]. This is complicated by the transient nature of the jet due to the impulsive start-
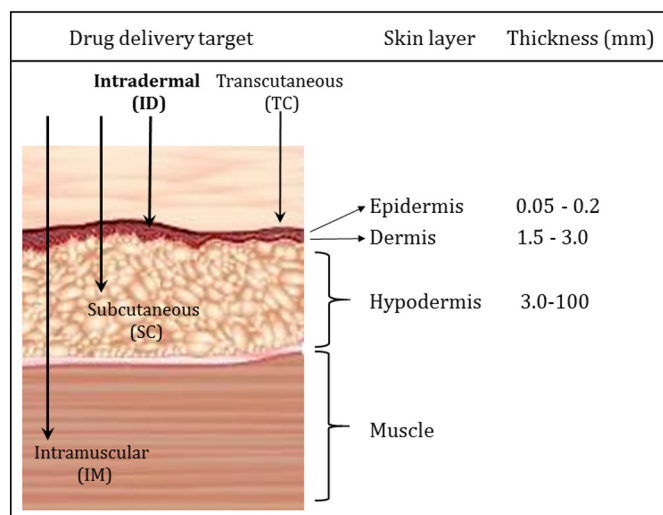

Fig. 1. Schematic of tissue layers and target regions for drug delivery.

up phase to pressurize the fluid. For understanding such complex fluid dynamics, it is important to address whether there is an optimal geometry which can give consistent performance irrespective of the fluid's rheological characteristics, or whether specific pairings of rheological profiles and tapers can be optimized.

In effort to understand the fluid dynamics of jet injection, there have been several analytical and numerical simulations studies [5,6,11,28–33]: An analytical study of spring-powered jet injector by Baker et al. [5] neglected both viscous and turbulence forces, reducing the problem to Bernoulli's equation and mass conservation equation. This approach resulted in force balance equations for the plunger movement and a set of partial differential equations which can give pressure variation inside the injection cartridge with respect to time. Another study [34] conducted a similar analysis with the consideration of a hydraulic loss parameter for water in Bernoulli's equation and found that initial oscillation due to impact force of the spring (impulse) decreases as the nozzle exit diameter increases. It was also found that the efficiency of jet injection (measured as the ratio of volume delivered to the volume expelled) of insulin in mice peaked for an orifice diameter 0.3mm [34].

Chen et al. [28] calculated jet exit velocity (at the orifice) by considering viscous loss forces and studied the effect of geometrical parameters on initial oscillations in jet pressure by measuring impact forces of liquid jets with a force sensor (transducer). The study found that peak jet pressure decreases with increase in injection volume or piston cross-sectional area while it increases with increasing spring constant [28]. In contrast, another study found that the fluid volume and injection chamber length does not affect the jet pressure profile, but affects the time duration of a jet injection [32]. It was also claimed that the stand-off distance between nozzle exit and surface of the force transducer does not have a substantial effect on the jet stagnation pressure profile [32], yet recent measurements [35] indicate otherwise.

A recent computational fluid dynamics (CFD) study showed no effect of varying fluid properties on the jet pressure profile but an increase in jet pressure with increase in orifice diameter for a conical tapering [31]. The limitation of their work is that the transient nature was given by pressure profile generated via a force transducer, whereas it can more accurately given by a plunger movement profile generated via high-speed videography [31]. An experimental study of both spring and laser-actuated liquid jets found that jets disperse more in air as nozzle exit diameter increases and as fluid viscosity decreases [12].

Stability analyses of liquid jets have revealed that the effects of velocity profile at the orifice, taper geometry, and fluid properties are all significant [36], which can be summarized through dimensionless numbers – principally – Reynolds number ($Re = \frac{\rho v d}{\mu}$), Weber number ($We = \frac{\rho v^2 d}{\sigma}$), and Ohnesorge number ($Oh = \frac{\sqrt{We}}{Re}$). The effect of these three dimensionless quantities on the type of liquid jet breakup in air is discussed extensively in the literature [12,36–38]. In particular, it is reported [37] that the orifice aspect ratio (L/D) and the cone angle of the taper have a significant effect on jet collimation and can be optimized for a particular set of fluid properties. It is also claimed [37] that rounding and polishing of internal surfaces maximizes liquid jet collimation in air.

In design of cartridge geometries for various rheological profiles, numerical simulations are particularly useful to achieve the optimal values of characteristics that can affect jet stability and collimation. However, these need to be guided by experimentally-determined values such as jet speed and pressure profile for efficient drug delivery into animal and human skins. For example, the effect of different nozzle diameters and jet velocities on the injection efficiency of mannitol delivery has been studied in both human and porcine skins [14], where the threshold velocity for a liquid jet to penetrate into the porcine skin is in the range of 80–100 m/s (for 152 μm jet diameter) whereas maximum injection efficiency in human and porcine skins is reported to occur in the range of 140–150 m/s for same jet diameter (nozzle exit diameter) [14]. Another study hypothesized that the injection efficiency of liquid jets can be modelled using a single parameter, the power of the liquid jet (P_{jet}) by combining two parameters such as nozzle exit diameter (d_o) and average liquid jet velocity ($\bar{v}_j$), and the relation can be given by [33] $P_{jet} = \frac{1}{8}\pi\rho d_o^2 \bar{v}_j^3$. The drug deposition depth in human skin was found to increase with increasing jet diameter or jet velocity and ellipsoid-shaped dispersions in the dermis occurred at 160 m/s with 152 μm jet diameter [33]. For a liquid jet power of about 50 W, the efficiency of delivery in the dermis was found to be above 90% [20].

Wendell et al. [8] found that the maximum power (at the impulsive start-up phase) of a liquid jet decides the penetration depth in murine tissue and follow-through average power (after impulsive jet start-up phase) only dictates the amount of fluid delivered in a certain period of time [8]. Baxter et al. [39] developed a theoretical model to predict hole depth and percentage of the expelled volume delivered into the dermis as a function of skin and jet characteristics [39]. Due to an increase in Young's modulus of the skin, decrease in intradermal injection efficiency and target drug delivery depth is reported [39]. A human cadaveric study found an increase in penetration depth into the skin due to the increase in the liquid jet stagnation pressure, but reported that the Young's modulus of live human skin is about twice that of cadaveric skin [9].

Through summarizing the studies above [3], the expected velocity for maximizing injection efficiency into the intradermal region is found to be $v_j \approx 150$ m/s for nozzle exit diameters of $d_o \approx 150$ μm. These values are therefore used to guide the present study to understand the role of rheology and geometry on the fluid dynamics of flow in tapered orifices. We perform numerical simulations to determine the pressure drop, exit velocity profile and boundary layer development for a range of Newtonian fluid viscosities and non-Newtonian fluids obeying the Carreau model.

2. Methods

2.1. Experimental

To validate our numerical results, we performed a limited experimental investigation to determine the upstream static pressure (P) as a function of jet flow rate (Q) and fluid viscosity (μ), from which we can calculate the average jet exit velocity at the orifice, $\bar{v}_j = \frac{4Q}{\pi d_o^2}$ and corresponding jet Reynolds number, $Re = \rho \bar{v}_j d_o / \mu$. The experimental setup is shown schematically in Fig. 2. Although spring-powered jet injection is transient in nature, we found that jet velocity is constant for the
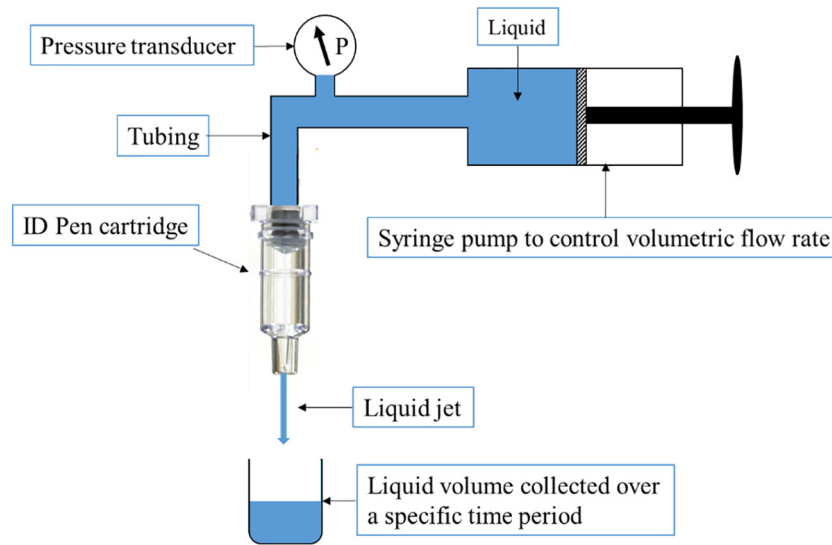
Fig. 2. Schematic representation of the experimental set-up (not to scale).

majority portion of the time for a complete jet injection [35]. Therefore, the jet injection system is in pseudo-steady state and assumption of steady state analysis is valid. In the experimental setup, a syringe pump is used to generate a steady fluid flow through a cartridge and upstream pressure is measured by pressure transducer as shown in Fig. 2. The steady flow through the cartridge is ensured with the help of real-time pressure reading from pressure transducer.

The specific injection cartridge used for these experiments is taken from the Bioject® Intra-Dermal (ID) pen™, which is a multi-tier tapering from an upstream inner diameter of 4.57 mm down to a nozzle exit diameter of 157 μm (± 2 μm). The geometrical shape can be found in Fig. 3b. The cartridge is firmly fitted with vacuum tubing to a syringe pump (PHD 2000) to drive the flow, and an in-line pressure transducer (Omega PXM409-USBH) to measure the static pressure upstream. The accuracy of the pressure based upon multiple readings was less than $+/-$ 2%. The volumetric flow rate was determined gravimetrically using a graduated cylinder to collect fluid over a specific time period.

Four different Newtonian fluids are used to achieve a wide range of Reynolds number values for validation of numerical simulation results.

Table 1
Physical properties of Newtonian liquids used in experiments and simulation conditions. The glycerin solutions are presented as concentration in terms of %(w/w) in water.

Fluid	Density ρ (kg/m^3)	Viscosity μ (Pa.s)
Water	996	0.001
50% Glycerin	1130	0.0069
60% Glycerin	1156	0.0137
70% Glycerin	1182	0.0296
80% Glycerin	1209	0.084
90% Glycerin	1235	0.215
95% Glycerin	1248	0.482
100% Glycerin	1261	1.31

These four fluids are 1) water, 2) 50% glycerine 3) 60% glycerine and, 4) 80% glycerine, whose physical properties are shown in Table 1, along with other fluids used in numerical simulations conditions. For varying percentages of glycerine in water (%w/w) from 0 to 100%, we
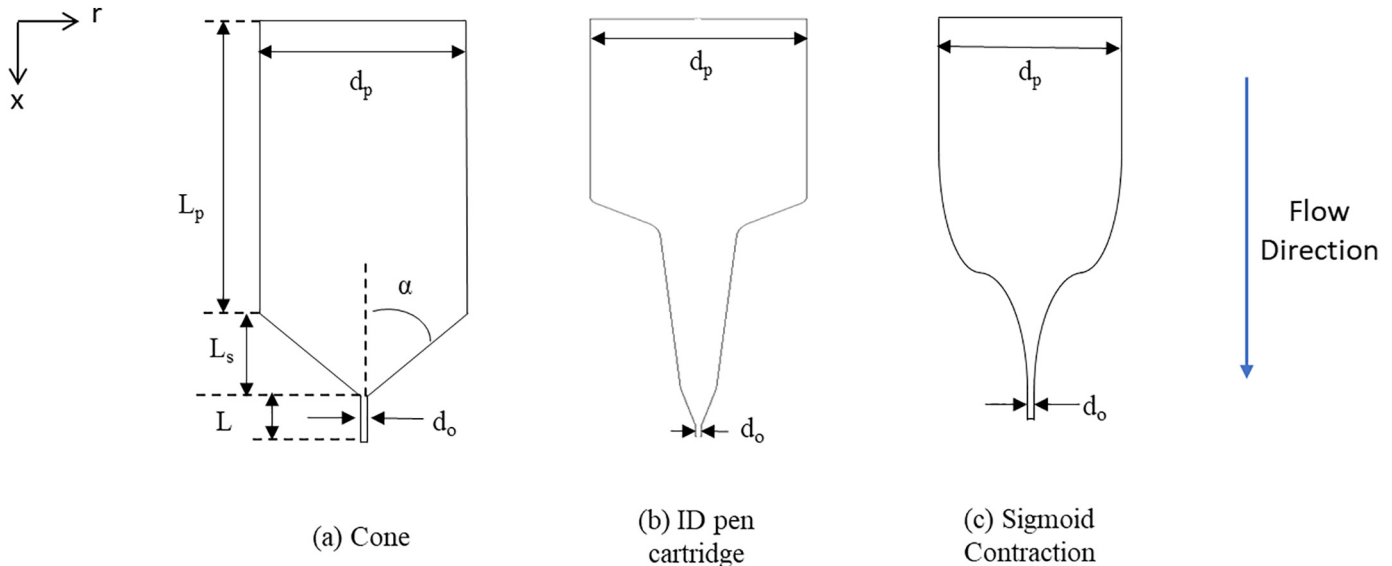

Fig. 3. Cartridge Geometries used for simulations. For all geometries, inner cartridge diameter d_p = 4.572 mm, and nozzle orifice diameter d_o = 157.4 μm. (a) Conical taper geometry with cone angle $\alpha = 10^o - 90^o$, L is the orifice length, L_p is the straight length of the cartridge body region, and L_s is the slanted cone height. (b) ID Pen cartridge geometry provided by Inovio Pharmaceuticals. (c) Sigmoid contraction geometry given by Richard's function (Eq. (4)). (Not to scale).

used ultrapure milliQ water and pure glycerine solution (Macron Fine Chemicals). Dynamic viscosity for Newtonian fluids in Table 1 is measured using a rheometer (DHR3, TA Instruments) at room temperature.

2.2. Numerical simulations

2.2.1. Overview of numerical approach

The simulation package used in this study was ANSYS FLUENT (version 18.2), which implements cell-centred finite volume method for calculating numerical solutions. Since the shear layer development and the orifice exit profile dictate jet collimation, we approach the numerical simulations using a single-phase analysis. We also assume the system is isothermal, incompressible, and neglect gravitational forces. The force required to overcome friction between the rubber plunger tip and the cartridge wall, for steady motion is < 1 lb. (4.4 N). Whereas the force required to overcome fluid viscous friction to generate a 150 m/s liquid jet from ID pen geometry varies from 50 N to 625 N over a range of viscosities. Hence, the frictional losses are excluded from current analysis. As justified in section 2.1, we use steady flow, which approximates the large portion of the actual injection. Furthermore, by performing several preliminary simulations, we also found no difference between three-dimensional and two-dimensional axisymmetric simulation results and so, for improved computational efficiency, we pursued 2D axisymmetric simulations. As shown in Fig. 4, a varying mesh size is used to achieve a high density of mesh points (~ 630 /mm) in the nozzle exit region whereas a low density of mesh points (~ 22 /mm) was used in the upstream cartridge region. For all geometries, the total number of mesh elements is below 20,000 to minimize the computational load and, the largest mesh element size is 50 μm to maximize accuracy.

The fundamental governing equations in the numerical simulation method are the continuity and Navier-Stokes equations (Eq. (1)), which are used for mass and momentum conservation respectively, inside the given geometrical domain, whilst the SIMPLE (Semi-Implicit Method for Pressure Linked Equations) model is used to solve the pressure-velocity coupled equations. Solution convergence is ensured by maintaining RMS residual value of at most 1e-06 for all cases. Additional information about the solution method used in numerical simulations is given in supplemental information.

For high-viscosity solutions (μ > 6.9 mPa.s), we perform laminar simulations since the maximum Reynolds number in the system is well below the turbulent flow regime (Re < < 4000). However, for lower viscosities in the inertial regime (Re > 4000), turbulent flow simulations were implemented with the RNG k-ε model [40,41], where the convergence of numerical results is determined by the residuals of the turbulent kinetic energy (k) and turbulence dissipation rate (ε).

The key parameters studied were flow rate through the nozzle orifice, fluid physical properties (summarized in the Reynolds number (Re) range of 10 to 30,000), fluid rheology and cartridge geometry, described in detail below. A key result of the numerical studies is the pressure drop (ΔP), which is non-dimensionalized as Euler number ($Eu = \frac{\Delta P}{\frac{1}{2}\rho \bar{v}_j^2}$), along with the exit velocity profiles and boundary layer thickness. A characteristic curve of Euler number versus Reynolds number provides a concise way to represent the system flow characteristics for a particular cartridge geometry.

2.2.2. Rheological profiles

Since many macromolecular suspensions, such as DNA vaccines, can be both high-viscosity and shear-thinning, a key focus of this study was the fluid rheological profile. Regardless of the fluid rheological model, the continuity and momentum conservation equations are given by:
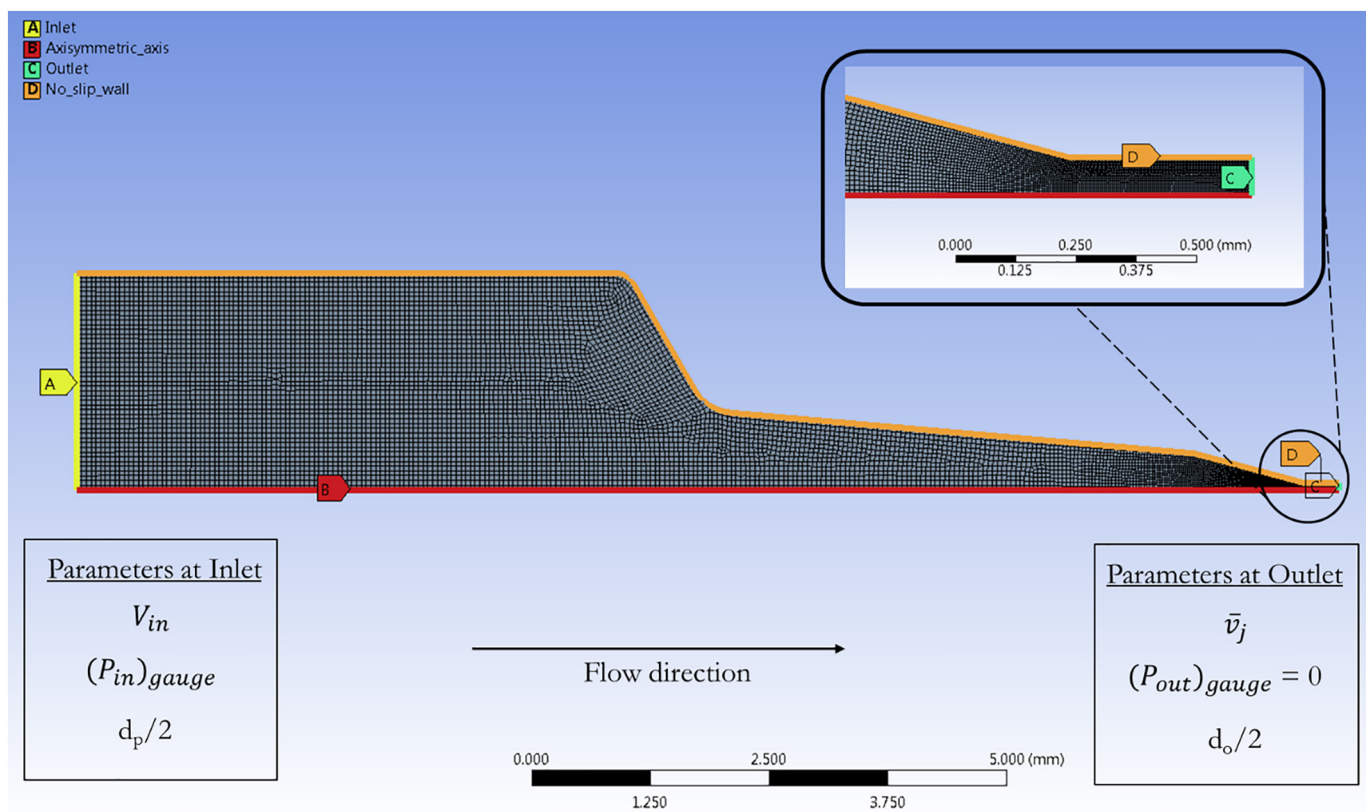
Fig. 4. Meshing setup for fluid flow through the ID pen cartridge geometry. Inset plot shows zoomed-in section of meshing near orifice exit. 'Meshing' software in ANSYS Fluent V18.2 is used to generate a fine mesh grid for all cartridge geometries. No-slip boundary condition is used at walls, while 'velocity-inlet' and 'ambient pressure outlet' boundary conditions are used at the inlet and outlet respectively.

$$\nabla \bullet u = 0, \ \rho \, u \bullet \nabla \ u = -\nabla P + \nabla \bullet \sigma \tag{1}$$

Where the stress tensor, σ, is given in terms of the rate-of-strain tensor, $\dot{\gamma}$, and apparent viscosity, μ_a:

$$\sigma = \mu_a(\dot{\gamma}) \ \dot{\gamma}, \ \dot{\gamma} = \nabla \ u + \nabla \ u^T, \ \dot{\gamma} = \sqrt{\frac{\dot{\gamma} : \dot{\gamma}}{2}} \tag{2}$$

For the apparent viscosity determination, we employed the Carreau model, which provides a physical description of a broad range of polymer solutions:

$$\mu_a = \mu_\infty + (\mu_0 - \mu_\infty)[1 + (\lambda \dot{\gamma})^2]^{\frac{n-1}{2}} \tag{3}$$

Where, μ_∞, μ_0, n, λ represent the infinite-shear viscosity, zero-shear viscosity, rate index, and relaxation time, respectively. To mimic the rheological profile of the macromolecular suspensions, Carreau model parameters for low concentrations of sodium carboxymethyl cellulose (CMC) solutions can be used, due to CMC's widespread commercial availability and extensive characterization in the literature [42,43]. Although the Carreau model parameter values in Table 2 do not represent any particular physical fluid, they are within a practical range of values observed [35,44,45] for low concentrations ($0.125\%_{(w/w)}$ - $2\%_{(w/w)}$) of aqueous CMC solutions. In Table 2, each row represents the set of parameter values used for simulation cases, where only one of the three parameters is varied for each set. For the purposes of singling out individual factors such as rate index, the other parameters were held constant, and in all cases the infinite shear rate viscosity was set as $\mu_\infty = 0.001$ Pa.s.

2.2.3. Geometries

For this study, we focused on three distinct geometries, as shown in Fig. 3: (a) Conical taper, (b) Bioject® ID Pen™ cartridge (referred as ID Pen cartridge), and (c) Sigmoid contraction/taper. Plunger diameter (d_p) is kept fixed at 4.57 mm to have the compatibility with current plunger design (ID Pen cartridge plunger). Nozzle orifice diameter of $d_o = 157$ μm (as per the ID pen geometry) is chosen to maximize intradermal drug delivery based on existing literature [3,9,14,20,33,39,46]. The velocity magnitude value at the inlet (V_{in}) is calculated accordingly to produce an average outlet jet velocity ($\bar{v}_j$) of either 50, 100, 150, or 200 m/s. Unless otherwise stated, the results herein pertain to an orifice length of L = 381 μm, corresponding to the aspect ratio $L/d_o = 2.42$, which corresponds to the ID Pen cartridge design.

For thorough experimental validation, we performed numerical simulations with the ID pen cartridge geometry across a range of Newtonian fluid viscosities 0.001–1.3 Pa.s and flow rates 0.97–3.9 ml/s corresponding to jet exit velocities of 50, 100, 150 and 200 m/s. For all the other cartridge geometries, a flow rate of 2.92 ml/s corresponding to jet exit velocity of 150 m/s is chosen as the simulation condition for all Newtonian and non-Newtonian fluids. The rationale behind selection of jet exit velocity of 150 m/s as a simulation condition is discussed in Section 1.

The sigmoid-type contraction in Fig. 3c can be generated by a generalized logistic function or Richard's function as given in Eq. (4), which gives the entire cartridge geometry outline with an asymmetric sigmoid contraction [47].

$$d(x) = \frac{d_p - d_o}{(1 + (\delta - 1) * e^{-k*(x - x_0)})^{\frac{1}{\delta - 1}}} + d_o \tag{4}$$

In Eq. (4), d(x) gives the outline of cartridge geometry along the axial direction (x-direction) and x_o dictates the inflection point in axial direction. Parameters 'k' and 'δ' determine the slope of taper and the inflection point in the radial direction (r) respectively.
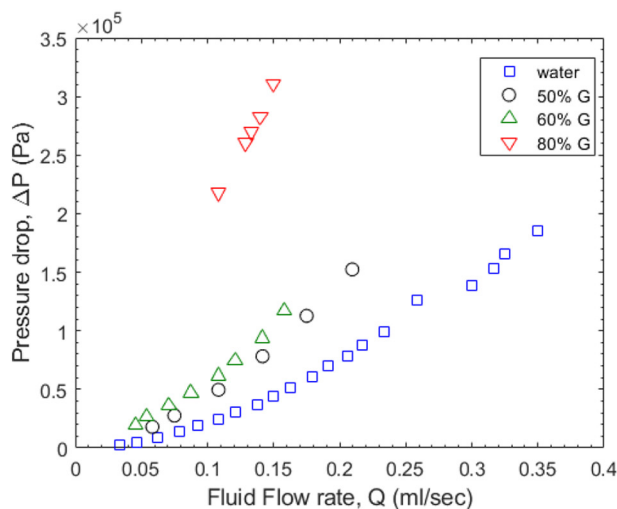
Fig. 3 shows the outline of the cartridge geometries studied in this paper. To reduce computational load, 2D axisymmetric cartridge geometries are used in the numerical simulations. Fig. 4 indicates the boundary conditions and the meshing setup used for ID pen cartridge geometry. The value of upstream pressure (($P_{in})_{gauge}$) is computed as an area-weighted average of pressure at the inlet surface. Similarly, quantities such as average fluid velocity at inlet (V_{in}) and average exit jet velocity at outlet ($\bar{v}_j$) are calculated. The total pressure drop across cartridge is computed across inlet and outlet of entire geometrical domain (i.e. $\Delta P = (P_{in})_{gauge}$) as shown in Fig. 4. In both experimental and numerical simulation methods, given pressure reading represents gauge pressure.
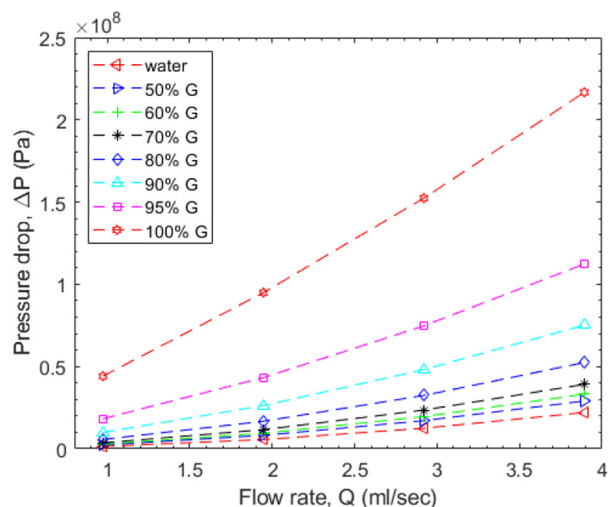
3. Results

3.1. Comparison with experiments

For validation of the simulations results, we first present the raw experimental data for upstream pressure measured as a function of flow rate for the four fluids (water, 50% glycerin, 60% glycerine, and 80% glycerine), shown in Fig. 5a. These measurements were taken using the ID Pen cartridge taper ($d_o = 157$ μm, $L/d_o = 2.42$). As expected, the data shows the pressure drop increasing with both flow rate and viscosity. For this particular geometry, over the range of flow rates 0.034–0.35 ml/s, the resulting upstream pressures are 2.76–185.47 kPa for water. Whilst the highest pressure drop was found with 80% glycerin and the flow rate of 0.15 ml/s at just over 300 kPa. For the same geometry, numerical simulations were performed across a range of Newtonian fluid viscosities 0.001–1.3 Pa.s (corresponding to water and 100% glycerin, respectively) and flow rates 0.97–3.9 ml/s. As per Fig. 5b, the numerical simulation results for these cases show upstream pressures in the range 1.45–216.74 MPa. From Fig. 5b, we find, as expected, that pressure drop across the geometry increases monotonically as the fluid viscosity or volumetric flow rate increases. To facilitate a straightforward comparison of these data, we present both results in the form of Euler number $\left(Eu = \frac{\Delta P}{\frac{1}{2}\rho \bar{v}_j^2} \right)$ versus Reynolds number $\left(Re = \frac{\rho \bar{v}_j d_o}{\mu} \right)$ in Fig. 5c.
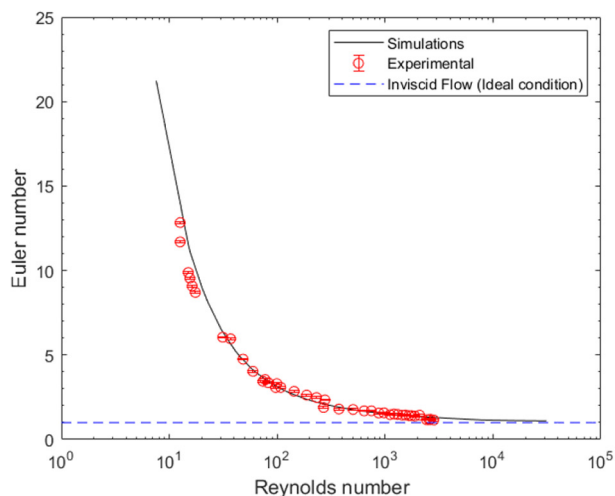
The experimental data in Fig. 5c shows experimental accuracy using error bar. An uncomplicated experimental setup for generating a steady flow using a syringe pump and measuring inline gauge pressure using an advanced pressure transducer allows us to reduce experimental errors to 1% - 2%. For wide applicability of our model over a range of

Table 2
Carreau Model parameters used in the simulation conditions.

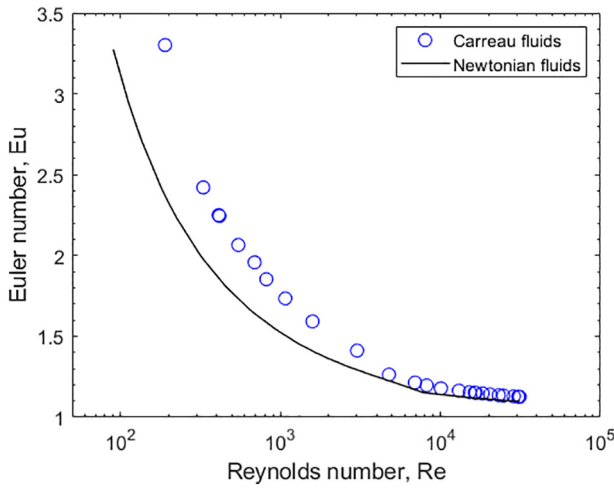| Carreau model parameter variation	λ (s)	μ_0 (Pa.s)	n
Zero-shear viscosity variation	0.1	1,3,6,8,10	0.4
Zero-shear viscosity variation	1	1,3,6,8,10	0.7
Zero-shear viscosity variation	1	0.003,0.0228,0.1732, 3,6,8,10	0.4
Relaxation time variation	0.001,0.01,0.1	1	0.7
Relaxation time variation	0.001,0.01,0.1,10	1	0.4
Rate index variation	1	1	0.1,0.25,0.55,0.7,0.4,0.8,0.9

(a)

(b)

(c)

Fig. 5. Pressure drop across injector cartridge for Newtonian fluids in the ID pen cartridge geometry. (a) Experiments: Pressure drop versus flow rate for different glycerine solutions (%G) (b) Simulations: Pressure drop versus flow rate for different glycerine solutions (%G) (c) Comparison of Euler number versus Reynolds number for both simulations and experiments.

fluid rheological parameters, validation of numerical simulations is performed using dimensionless quantities (*Eu* vs *Re*) instead of dimensional quantities (ΔP vs Q) [26]. The agreement between experimental data and simulation data is very good with normalized mean square error (NMSE) of 2.61% across the span of experimental data. This plot reveals that the Euler number decreases rapidly in the range $10 \le Re \le 100$, and then gradually asymptotes toward the inviscid limit of $Eu \equiv 1$. For a physical interpretation of Fig. 5c, the inverse of Euler number can be thought of as the nozzle mechanical efficiency of conversion of upstream pressure energy to kinetic energy of the jet, meaning that the system becomes more efficient at high Reynolds numbers, approaching the inviscid limit as $Re > 10^4$ due to reduced viscous loss through the nozzle. At $Eu = 1$, an upstream pressure energy provided to the system will completely convert into the kinetic energy of a liquid jet coming through the nozzle exit. Experimental results show us a minimum Euler number of 1.153 at 0.35 ml/s for water ($Re \sim 2827$) whereas a maximum Euler number of 12.84 at 0.108 ml/s for 80% glycerine ($Re \sim 12.59$). For ID pen cartridge simulations data, lowest Euler number of 1.098 occurs at 3.89 ml/s for water ($Re \sim 31,340$) whereas highest Euler number of 21.23 occurs at 0.973 ml/s for 100% glycerin ($Re \sim 7.57$). On further analysis, we found that the nozzle mechanical efficiency decreases with an increase in viscosity or decrease in flow rate, within the range of parameters studied here. From Fig. 5c, it is also found that the majority (98%) of the total reduction in Euler number occurs below Reynolds number of 1000, where it decreases inversely with Reynolds number. This suggests that the viscous dominated flow at low Reynolds number has more significant impact on maximizing nozzle mechanical efficiency than inertial dominated flow at high Reynolds number. Due to the dominant viscous flow inside the cartridge, it is important to study the effect of fluid rheology on nozzle mechanical efficiency, especially for non-Newtonian fluids.

3.2. Effect of fluid rheology

Given the excellent quantitative agreement between experiments and simulations for the ID Pen geometry, and to provide a fair comparison, we now proceed to examine the effect of fluid rheology in this same geometry (Fig. 3b). The same protocol is followed by setting the inlet velocity corresponding to an average jet exit velocity of 150 m/s, whilst the effect of each parameter in the Carreau model on pressure drop is studied individually as per Table 2. To study the effect of Carreau model parameters, each of three parameters were varied independently while keeping others constant as per Table 2. The characteristic curve of Euler number versus Reynolds number can be plotted for Carreau fluids using a generalized Reynolds number (Re_{gen}), which is given as [48]:

$$Re_{gen} = \frac{\rho u d_o}{\frac{(\mu_0 - \mu_\infty)\left(\frac{3n'+1}{4n'}\right)}{\left(1 + \left(\lambda\left(\frac{3n'+1}{4n'}\right)\frac{8u}{d_o}\right)^2\right)^{\frac{1-n}{2}}} + \mu_\infty\left(\frac{3n'+1}{4n'}\right)}$$

(5)

Fig. 6. Fluid rheological effect on Euler number vs. Reynold number at nozzle exit (Generalized Re for Carreau fluids). Geometry: ID pen cartridge. For Carreau fluids, $\bar{v}_j = 150$ m/s.

$$n' = \frac{\frac{8u}{d_o}\left[\mu_\infty - 2\lambda^2(\mu_0 - \mu_\infty)\frac{1-n}{2}\left(\frac{8u}{d_o}\right)^2\left(1 + \left(\lambda\frac{8u}{d_o}\right)^2\right)^{-\left(1-\frac{1-n}{2}\right)} + \frac{(\mu_0 - \mu_\infty)\left(1 + \left(\lambda\frac{8u}{d_o}\right)^2\right)^{-\left(\frac{1-n}{2}\right)}}{}\right]}{\mu_\infty\frac{8u}{d_o} + (\mu_0 - \mu_\infty)\frac{8u}{d_o}\left(1 + \left(\lambda\frac{8u}{d_o}\right)^2\right)^{-\left(\frac{1-n}{2}\right)}} \quad (6)$$

Eq. (5) gives generalized Reynolds number for Carreau fluids in terms of fluid density, Carreau model parameters, nozzle orifice diameter (d_o) and, fluid velocity ($u = \bar{v}_j$). Each individual point in Fig. 6 represents a simulation case of a Carreau fluid with model parameters given in Table 2. The generalized Reynolds number in Eq. (5) does not consider the shear rate profile or geometrical variation inside the cartridge, and the only geometrical parameter used in Eq. (5) is the nozzle orifice diameter, which does not reflect the true variation in strain rate throughout the cartridge and nozzle. This notwithstanding, for both types of fluid in Fig. 6, we see the inverse proportionality between Euler number and Reynolds number along with the transition from a viscous-dominated flow to an inertial-dominated flow.

Throughout the range of Reynolds number in Fig. 6, Carreau fluids have higher Euler number than Newtonian fluids at corresponding Reynolds number. The % increase in Euler number from Newtonian fluids to Carreau fluids changes from 2.51% at $Re \sim 31{,}320$ to 39.31% at $Re \sim 190$. At constant $\bar{v}_j = 150$ m/s, Fig. 7 reiterates this difference in terms of viscosity at the nozzle exit. Apparent viscosity for Carreau fluids in Fig. 7 is based on averaged shear rate across the node values at the nozzle exit and can be denoted as $(\bar{\mu}_a)_{d_o}$. This also provides an alternative way to calculate the Reynolds number for Carreau fluids at the nozzle exit as opposed to generalized Reynolds number (Re_{gen}) in Eq. (5), and generally the agreement with the Newtonian data is slightly improved, however, for consistency with literature, we adopt the convention of Eq. (5).

The shear-thinning rheological behaviour dictates that apparent viscosity decreases with an increase in shear rate. Thus, in low-shear regions $\dot{\gamma} \sim O(10^1)$, i.e. upstream cartridge, the apparent viscosity is higher and varies more than in the taper or orifice regions. To expound, the absolute range of apparent viscosities $(\bar{\mu}_a)_{d_o}$ at the orifice changes from 0.001 Pa.s to 0.215 Pa.s (see Fig. 7), whilst the corresponding variation in apparent viscosity, μ_a, across the rest of the cartridge geometry increases from $\mu_a \sim 0.003$ Pa.s to $\mu_a \sim 0.81504$ Pa.s. In contrast, the viscosity for Newtonian fluids remains constant throughout the cartridge geometry. As such, the discrepancy in Euler
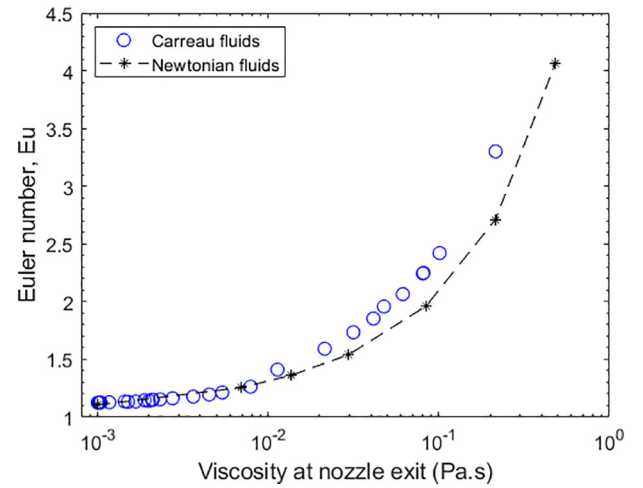
Fig. 7. Euler number variation with viscosity at nozzle exit. Newtonian fluids viscosity range – (0.001 to 0.482 Pa.s). Carreau fluid viscosities are given by $(\bar{\mu}_a)_{d_o}$. Geometry: ID pen cartridge. $\bar{v}_j = 150$ m/s.

number between Carreau fluids and Newtonian fluids at higher $(\bar{\mu}_a)_{d_o}$ in Fig. 7, can be explained by the higher μ_a within the cartridge geometry. The supplemental information contains detailed μ_a contours for ID pen cartridge at both extremes of $(\bar{\mu}_a)_{d_o}$ in Fig. 7.

Although the data in Figs. 6 and 7 show that Carreau fluids have higher Euler number than Newtonian fluids for corresponding Reynolds number, to fully appreciate the influence of rheological behaviour, it is instructive to single out the effect of shear-thinning degree via rate index (n), all else being equal. At rate index $n = 1$, Carreau fluids become Newtonian with viscosity $\mu_a = \mu_o$. For constant $\mu_o = 1$ Pa.s, Fig. 8 shows clearly that shear thinning behaviour of Carreau fluids is highly advantageous in regards to increasing the mechanical efficiency ($Eu \leq 3.4$) when compared to the Newtonian counterpart ($Eu \approx 8$). The principal reason for reduction of Euler number for Carreau fluids in Fig. 8 is the high shear region near the orifice (shown in Fig. 17), where $\dot{\gamma} \sim \frac{\bar{v}_j}{d_o} \sim O(10^6)$, rendering apparent viscosities close to the infinite rate value ($\mu_\infty \approx 0.001$ Pa.s), in all cases for $n \leq 0.7$. This reduction of apparent viscosity in the high-shear region has a significant impact on minimizing the pressure losses inside the cartridge geometry and therefore, Euler number. On further analysis, we found that Euler number increases with increase in zero-shear viscosity (μ_0) or with
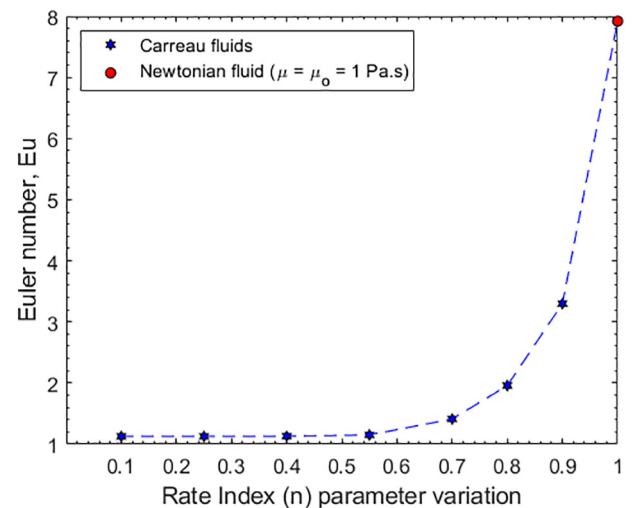
Fig. 8. Euler number vs. rate index parameter in Carreau model. $\mu_0 = 1$ Pa.s, $\mu_\infty = 0.001$ Pa.s, $\lambda = 1$ s. Geometry: ID pen cartridge. $\bar{v}_j = 150$ m/s, $d_0 = 157.4$ μm.

decrease in relaxation time (λ). Therefore, to achieve maximum nozzle efficiency, the apparent viscosity should be as low as possible, especially in the high shear region near the nozzle exit. Supplemental information contains plots of Euler number versus μ_0 and λ.

Although the strain rate profile inside the entire cartridge contributes to the viscosity variation and total pressure drop, strain rate profile near the nozzle exit is the most important deciding factor in determination of the total cartridge pressure drop and thus, nozzle mechanical efficiency. As such, it is clear that the high shear due to the tapering and restriction at the nozzle orifice dominates, hence it is instructive to analyze the role of tapering region in cartridge geometry.

3.3. Effect of geometry

3.3.1. Conical taper - effect of cone angle

Geometrical parameters have a significant impact on jet collimation and stability [37,49–53] and upstream pressure [26] required to achieve a high-velocity jet. Therefore, we now focus on a simple conical taper to elucidate certain features. Fig. 3a gives a visual description of geometrical shape and parameters studied for conical cartridge geometry.

Although all the simulations are solved using a steady state solver, the size of the geometrical domain considered for the fluid flow affects the pressure field inside the domain and therefore, the total volume of the fluid domain is set constant at $V = 0.1$ mL throughout this study. The cartridge length (L_p) for each cone angle geometry is given by $\frac{\pi D_p^3}{24 * tan\alpha} + \pi r^2 L_p = V$. All parameters except cone angle (α) and slanted cone height (L_s) are kept constant throughout the study of range of conical tapers.

From Fig. 9, we see that for all conical tapers, mechanical efficiency increases as Reynolds number increases in a similar fashion as the ID pen cartridge. The magnitude of variation in Euler number over the range of Reynolds number in Fig. 9 is much larger than the magnitude of variation due to change in cone angle at any particular Reynolds number. We clearly see that cone angle effect is less significant at low Reynolds number (~ 20–350), i.e. viscous-dominated flow, whereas it is more significant at high Reynolds number (~ 1000–25,000), i.e. inertial-dominated flow. This suggests that the turbulence losses in the inertial regime change more significantly with variation in cone angle as compared to the viscous losses. To further illustrate the effect of cone angle, Fig. 10 shows the Euler number vs. cone angle for different Newtonian fluids.

The geometrical outline transition from conical taper to straight nozzle orifice becomes more drastic as cone angle increases. For $Re \geq 940$, Eu continuously increases with increasing cone angle. This
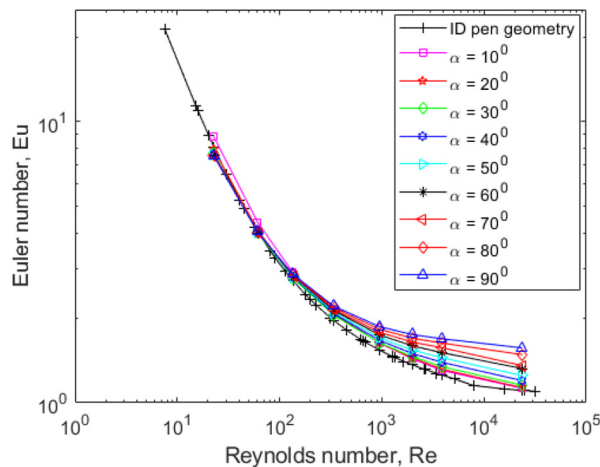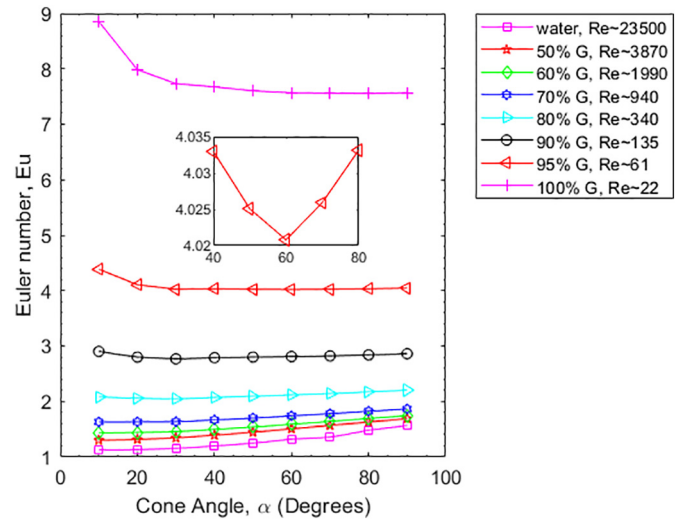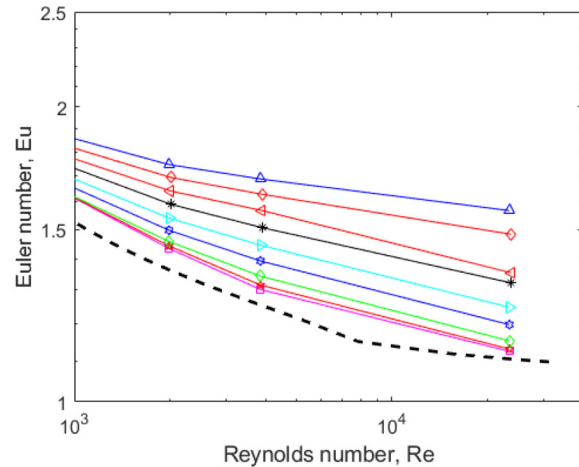

Fig. 10. Euler number versus cone angle (α) for different glycerin solutions (% G). In all cases $\bar{v}_j = 150$ m/s. Inset plot for 95% glycerin with x-y axes same as the outer plot.

pressure loss in the inertial-dominated regime can be explained by the increasing turbulence losses due to the abrupt changes in geometrical outline as cone angle increases.

A subtle aspect of the results in Fig. 10 is that there is a minimum in the Euler number as a function of cone angle, for $Re \leq 340$. For example, when $Re \sim 61$ (95% glycerine), inset plot in Fig. 10 shows a minimum Euler number at α = 60°. Similarly, Table 3 give the cone angles, at which the minimum Euler number occurs for each Newtonian fluid. Whilst the percentage difference between minimum and maximum Euler numbers shown in Fig. 10 inset plot is 0.3%, the absolute reduction in pressure drop across the cartridge is approximately 173 kPa, which could have a considerable impact on selection of spring-constant for spring powered needle-free jet injectors.

The Euler number is minimized at a particular cone angle for $Re \leq 340$ because the flow is accelerated toward the nozzle exit in a way that almost optimally reduces viscous losses and boundary layer growth. To elucidate the occurrence of minimum Euler number, we single out the case for 95% glycerin ($Re \sim 61$). For $Re \sim 61$, at α < 60°, the boundary layer grows due to comparatively higher overall cartridge length, which increases viscous friction and pressure loss across the cartridge. This causes pressure drop to be minimum at α = 60° in range of cone angles 10° ≤ α ≤ 60°. The slanted cone height

Fig. 9. (a) Euler number versus Reynolds number for Newtonian fluids in conical tapers with various cone angles (α = 10° – 90°). For ID pen cartridge, $\bar{v}_j = $ 50–200 m/s, whilst for all conical tapers, $\bar{v}_j = 150$ m/s. $L/d_0 = 2.42$. (b) Zoomed perspective of high-Re region.

Table 3
Cone angle for each Newtonian fluid, where minimum Euler number occur.

Fluid	α (degrees)
Water	10
50% Glycerin	10
60% Glycerin	10
70% Glycerin	10
80% Glycerin	30
90% Glycerin	30
95% Glycerin	60
100% Glycerin	80

$\left(L_s = \frac{d_p}{\tan(\alpha)}\right)$ for all conical nozzles is not kept constant and therefore, decrease in cone angle results in higher overall cartridge length $(L_s + L_p + L)$. For $Re \sim 61$, at $\alpha > 60°$, pressure losses increase because of the more sudden transition near the start and end of a conical taper. This sudden transition at $\alpha = 70°$ causes the formation of a recirculation zone at the sharp corner, shown in Fig. 11. The size of this recirculation zone increases for cone angle $\alpha > 70°$, which results in increased pressure losses. This results in a minimum pressure drop across cartridge at $\alpha = 60°$ in range of cone angles $60° \leq \alpha \leq 90°$.

Similarly, for $Re \geq 940$, $\alpha = 10°$ is found to have minimum Euler number, because in the inertially dominated regime, the pressure losses due to viscous boundary layer growth and viscous friction are negligible, whereas the pressure losses due to the sudden geometrical transition and recirculation zone are significant at higher α values. Amongst the parameters considered here, $\alpha = 10°$ provides the least abrupt geometrical transition and highest overall cartridge length and thus 10° cone angle geometry is best suited for inertially dominated flow.

### 3.3.2. Boundary layer development

In previous studies [36,37], it has been found that boundary layer thickness (BLT) has a major impact on liquid jet collimation, therefore we now consider the effect of different nozzle geometry on BLT over a range of Newtonian fluid parameters. The BLT determines the extent of flow development inside the nozzle; higher BLT suggests that flow is highly developed, and the velocity magnitude profile is almost parabolic in nature.
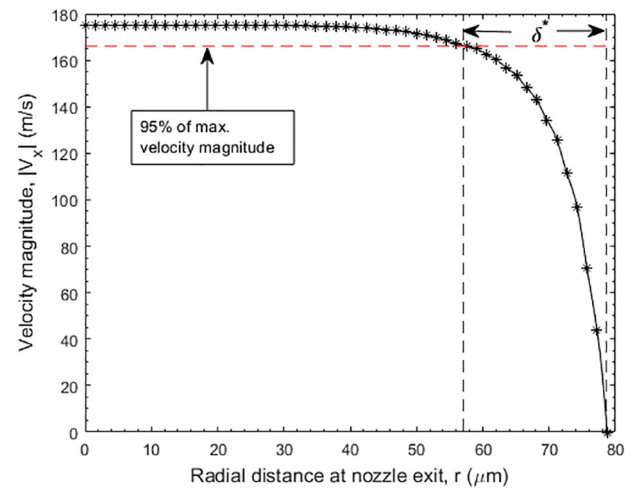
Fig. 12. Velocity magnitude profile at the nozzle orifice for 50% glycerin in a 10° cone angle with $\bar{v}_j = 150$ m/s (Re = 3866). The boundary layer thickness, δ* is evaluated at the nozzle orifice.

As depicted in Fig. 12, the BLT at the orifice is considered at 95% of the maximum velocity at nozzle orifice [54], because it neglects the small scale error in velocity magnitude values at any node on nozzle exit. The velocity magnitude profile is further refined using interpolation across the node values at the nozzle exit to increase the accuracy of BLT estimation.

Fig. 13 shows that BLT decreases with respect to an increase in Reynolds number for all cone angle geometries, and helps to explain the trends in Fig. 9, whereby only a small difference in Euler number was found at low $Re < 10$ [2], but a larger variation in Eu for higher $Re > 10$ [3]. This inverse proportionality between BLT and Reynolds number is analogous to behaviour of Blasius solution for boundary layer thickness for fluid flow over a flat plate. As Reynolds number is the ratio of viscous forces to inertial forces, high Reynolds number ($Re > 940$) system has comparatively lower viscous boundary layer growth and therefore low BLT at the nozzle exit. Conversely, the viscous boundary layer growth is higher at lower Reynolds number, which generates high BLT at the nozzle exit.
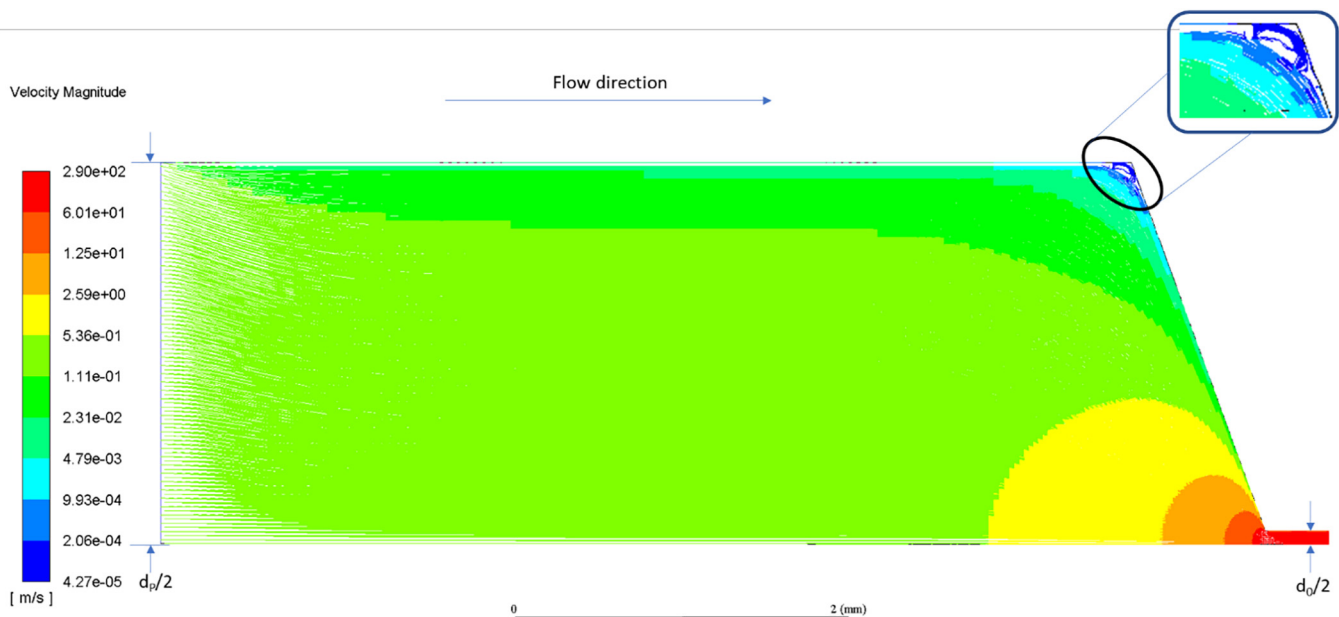
Fig. 11. Snapshot of velocity magnitude streamlines for 70° cone angle geometry and 95% glycerine solution. $\bar{v}_j = 150$ m/s. 2D axisymmetric plot from ANSYS (R18.2) Fluent. Logscale color plot to enhance vizualization in low velocity magnitude region.
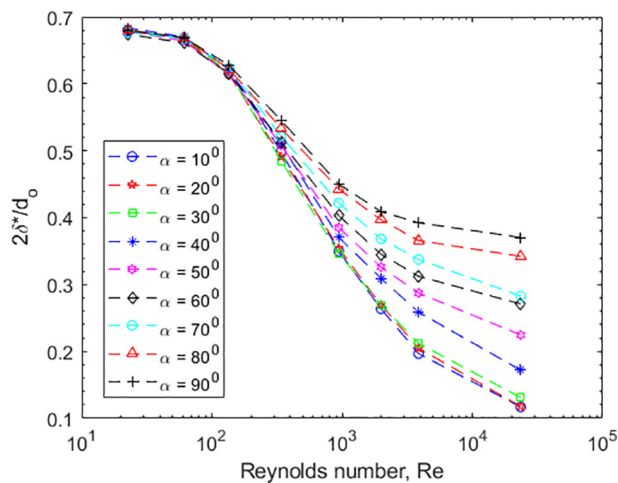
Fig. 13. Variation in BLT (δ^*) to nozzle exit diameter (d_o) ratio with respect to Reynolds number variation and cone angle (α) variation. Simulated for all Newtonian fluids from Table 1. $d_o = 157.4\ \mu m, \bar{v}_j = 150$ m/s.

From Fig. 13, we see that the magnitude of the effect of Reynolds number on BLT increases as cone angle decreases. In the inertial regime, the effect of cone angle on BLT is significant due to the flow separation phenomena as shown in Fig. 14. The flow streamlines as shown in Fig. 14 cannot abruptly change direction, especially for high Reynolds number flow. However, the converging flow streamlines follow the smooth transition path, where the streamlines squeeze through *vena contracta* [55] and expand thereupon. *Vena contracta* is defined as the point at which the local diameter of fluid streamlines is the least. In the inertial flow regime, at Re ~ 23,500 and $\alpha = 80°$ in Fig. 14, we can clearly see the occurrence of *vena contracta* in orifice region, which is responsible for the increase in BLT as cone angle increases. It has been reported that a low pressure region is created at *vena contracta* due to higher local fluid velocity, which can result in local cavitation or hydraulic flip [56,57]. Literature on liquid jets [36,37] reports that jet coherency increases as BLT at the nozzle exit decreases. Therefore, to achieve maximum liquid jet coherency
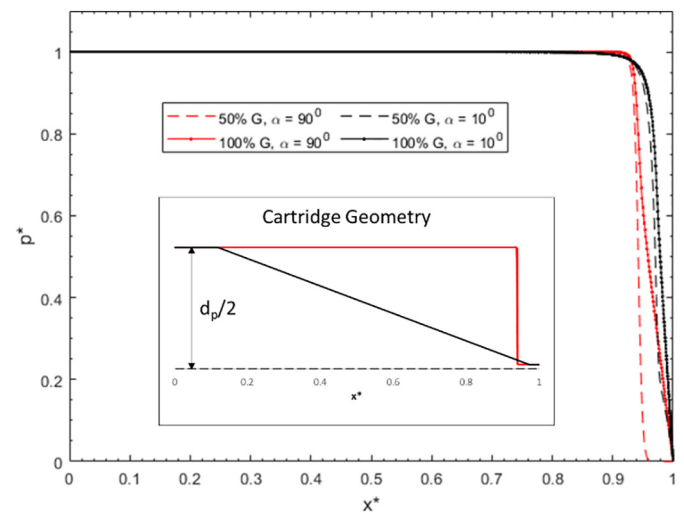

Fig. 15. Dimensionless gauge pressure (p^*) along axisymmetric axis versus dimensionless cartridge length (x^*) for different % glycerine solutions (%G) and cone angle (α) cartridge geometries as shown in inset plot (Red curve: $\alpha = 10°$, Black curve: $\alpha = 90°$). $\bar{v}_j = 150$ m/s. (For interpretation of the references to color in this figure legend, the reader is referred to the web version of this article.)

(collimated jet stream), flow parameters and the nozzle geometry should be chosen in a manner that minimizes BLT at nozzle exit.

3.3.3. Axial variation of pressure drop

To understand the effect of different fluid viscosities and cone angle geometries on pressure variation inside the cartridge, Fig. 15 presents dimensionless gauge pressure ($p^* = \frac{p}{p_{max}}$) along the x-axis versus dimensionless cartridge length ($x^* = \frac{x}{L_s + L + L_p}$) for cone angle cartridge geometries.

Gauge pressure inside a nozzle cartridge varies in axial direction from highest gauge pressure inside the system to zero, where a liquid jet is expelled out of the nozzle orifice into atmospheric pressure. In Fig. 15, we see the gauge pressure variation at two extremities of cone
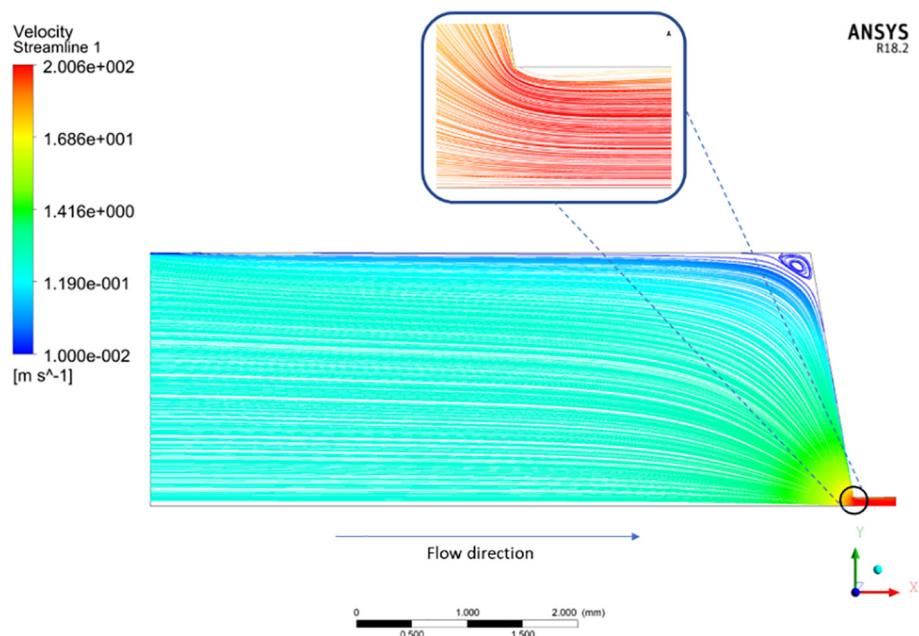
Fig. 14. Velocity streamlines for 2D axisymmetric nozzle. Simulation case of 80° cone angle geometry and water. $\bar{v}_j = 150$ m/s. Re ~ 23,500. Zoomed-in section of flow separation at the beginning of orifice.
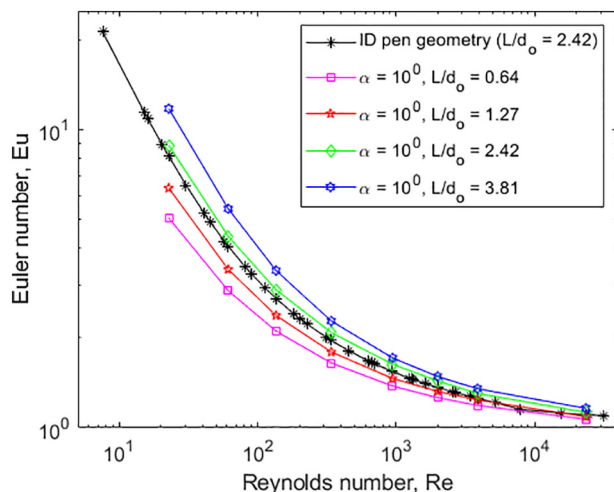
Fig. 16. Euler number versus Reynolds number for various orifice lengths (L) with cone angle = 10° and d_o = 157.4 µm. Simulated for all Newtonian fluids from Table 1. For ID pen cartridge, $\bar{v}_j$ = 50–200 m/s. For conical taper, $\bar{v}_j$ = 150 m/s.

angle nozzle geometries for two extremities of glycerine concentrations used in this study. For all the cases in Fig. 15, > 95% of the total pressure drop occurs in last 10% of cartridge length. This suggests that the high shear region near the orifice (Fig. 17) requires more attention in nozzle geometrical optimization than low shear region upstream, in order to maximize the mechanical efficiency of a nozzle. In particular, rounding of surfaces and reduction in abrupt changes in geometrical outline, have a significant impact on nozzle mechanical efficiency and liquid jet coherency. As such, the following sections consider the impact of orifice length and new sigmoid-type tapers.

3.3.4. Effect of orifice length

In previous section, we saw that the high shear region near the orifice is a very important contributing factor to the total cartridge pressure drop and therefore, the effect of orifice length (highest shear region as shown in Fig. 17) on Euler number is studied. To illustrate the effect of orifice length on pressure drop, the nozzle geometry of 10° cone angle is chosen, since in the inertial-dominated flow regime, it has lower BLT and lower Euler number than other cone angle nozzle geometries. In Fig. 16, we present the equivalent Eu vs. Re plot for four orifice lengths (L = 100, 200, 381, and 600 µm), corresponding to ratios L/d_0 = 0.64, 1.27, 2.42, and 3.81. here, we observe that pressure drop across the cartridge increases monotonically with the orifice length (L), throughout the range of Reynolds number.

As the orifice length increases, the BLT extends further [36,37], providing more resistance to the flow, and thus increasing the pressure

required to maintain the specified flow rate. In a similar fashion to the ID pen geometry, Eu reduces drastically in the viscous-dominated regime before it asymptotically decreases to reach pure inviscid flow condition, $Eu \rightarrow 1$ as $Re \rightarrow \infty$. Since the viscous friction is the dominant factor for the pressure loss, we see that the magnitude of the effect of Reynolds number on Euler number increases with the increase in the viscosity of a fluid.

In Fig. 16, for the same orifice length L/d_o = 2.42, 10° cone angle cartridge has 2%–9% higher Eu than ID pen cartridge over the range of Re studied. On the other hand, for the 10° cone angle cartridge with L/d_o = 3.81, Eu is 9%–132% higher than the cartridge with L/d_o = 0.64 over the same range of Re. This suggests that the pressure drop due to changes in orifice length i.e., high shear region is more significant than the pressure drop due to geometrical changes in low shear region. This is in accordance to results in Fig. 15, where we see that majority of the pressure drop occurs in high shear region, and evident from inspection of the strain rate profiles, an example of which is shown in Fig. 17. Here, we observe the variation in strain rate from $\dot{\gamma} \sim O(1)$ in the upstream region (d_p = 4.57 mm) to $\dot{\gamma} \sim O(10^7)$ near the orifice region (d_o = 157.4 µm).

Since the high shear region is responsible for most of the pressure losses, any straight orifice section in the nozzle geometry should be as low as possible to avoid reduction in mechanical efficiency. This may also induce jet dispersion, which can be either beneficial in regard to achieving reduced penetration depth into intradermal tissue, or deleterious if the goal is deep muscle injection.

3.3.5. Sigmoid contraction

An alternative, smooth taper geometry from can be can be achieved through a generalized logistic function such as Richard's curve function [47] given by Eq. (4), which generates an asymmetric sigmoid contraction from a fixed upper asymptote (upstream cartridge diameter) to a lower asymptote (nozzle orifice). It can also address the issues presented herein related to 1) pressure losses due to the recirculation zone due to abrupt change in geometry, 2) pressure losses due to the high overall cartridge length for low cone angle nozzle geometries, and 3) significant pressure losses due to the straight orifice section.

Out of five parameters in Richard's curve, only two parameters (k and δ) are varied based on heuristic approach to achieve six different outlines as per Fig. 18. At a constant δ = 0.9, the transition steepness from cartridge diameter (d_p) to nozzle orifice diameter (d_o) increases with k (e.g. yellow vs. green curves in Fig. 18). On the other hand, at a constant k = −1.5, increase in δ causes the overall cartridge length to increase, especially near the orifice region (e.g. dark blue vs. purple curves in Fig. 18).

Due to the decrease in orifice length, viscous boundary layer growth and viscous friction reduces throughout the range of Re, which causes Eu to decrease with decrease in δ as shown in Fig. 19. This suggests that δ should be minimal to minimize the pressure losses across the
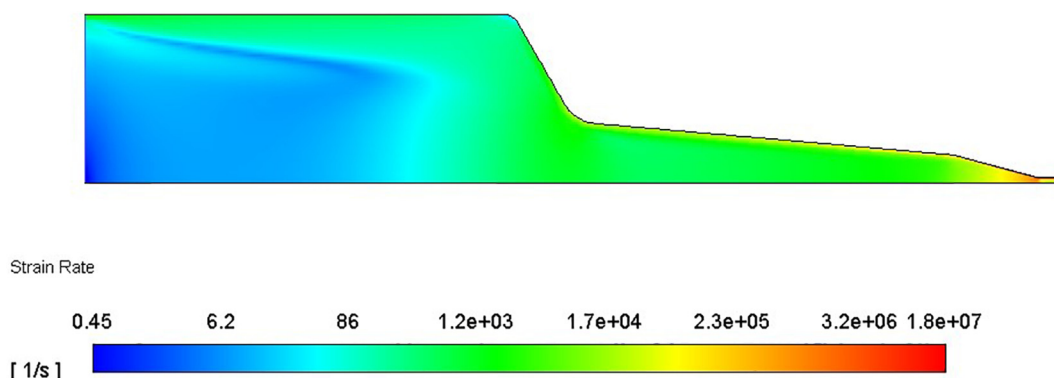
Fig. 17. Shear strain rate for 2D axisymmetric nozzle from ANSYS (R18.2) Fluent. Simulation case of ID pen geometry and water. $\bar{v}_j$ = 150 m/s.
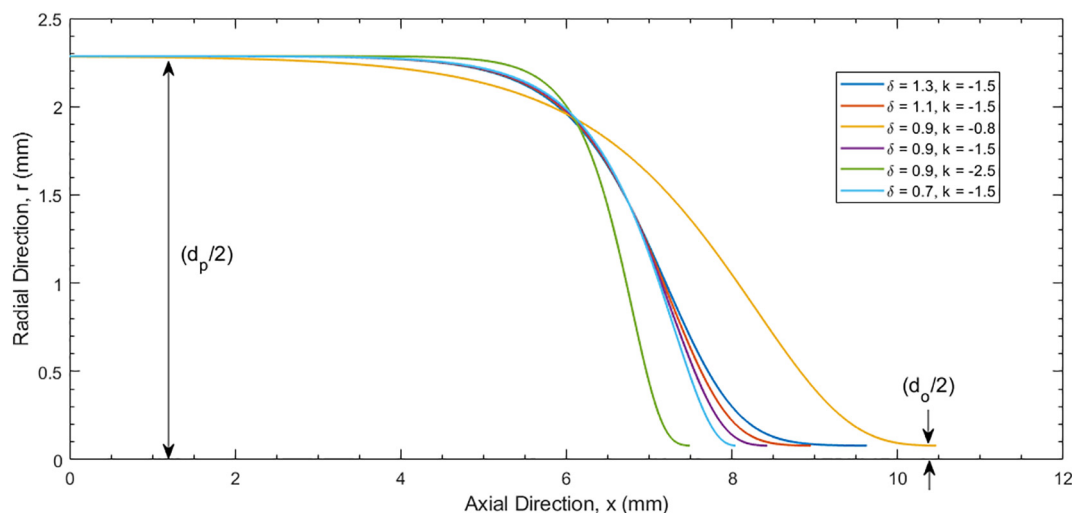
Fig. 18. Cartridge geometries from Richard's function all with d_p = 4.572 mm, d_o = 157.4 μm. Total cartridge volume for each geometry is fixed at 0.1 ml.
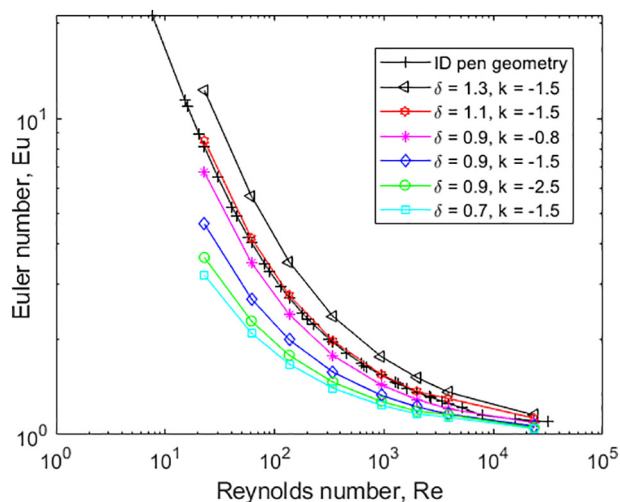

Fig. 19. Euler number versus Reynolds number for cartridge geometries in Fig. 18. Simulated for all Newtonian fluids given in Table 1. For ID pen cartridge, $\bar{v}_j$ = 50–200 m/s. For conical taper, $\bar{v}_j$ = 150 m/s.
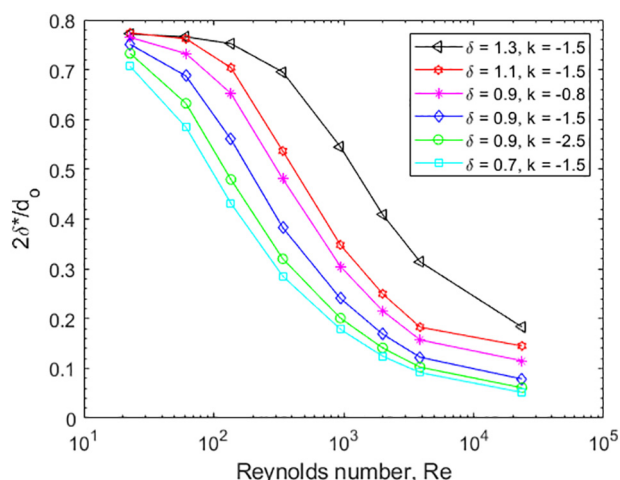

Fig. 20. Variation in normalized BLT (δ^*/d_o) with respect to Reynolds number, for Newtonian fluids in cartridge geometries from Fig. 18 with d_o = 157.4 μm, $\bar{v}_j$ = 150 m/s.

cartridge. For the same reason, we see a decrease in *Eu* with increase in *k* for all values of *Re*. The geometrical effect on *Eu* is more influential in the viscous-dominated region in a similar fashion as it is for orifice length in Fig. 16. In accordance with BLT development in conical tapers, Fig. 20 also reveals that the pressure loss reduction at high *Re* values is due to suppression of boundary layer growth. However, the sigmoid contractions are clearly superior in terms of mechanical efficiency at higher *Re*.

The literature [3,14,19,29,30,33,46,58] on jet velocity impact on tissue penetration have mainly focused on controlled variation in axial jet velocity (axial momentum). At the same input spring force, proposed sigmoid cartridge geometries can be designed to produce different axial jet velocities. Pressure drop (ΔP) inside the cartridge geometry can be controlled by changing high-shear and low shear regions inside the cartridge. For a fixed gauge pressure at inlet (i.e., fixed spring force), low Euler number cartridge geometry will have more jet kinetic energy at nozzle exit as compared to the cartridge with high Euler number. This increased kinetic energy (jet velocity) in axial direction will result in higher tissue penetration depth [33].

The last important quantity pertaining to jet collimation is the velocity angle at the orifice, especially since Richard's function does not ensure parallel walls at the nozzle exit. The velocity angle (θ) can compare the radial velocity magnitude ($|V_r|$) to axial velocity magnitude ($|V_x|$) at the nozzle exit by $\theta = tan^{-1}\left(\frac{|V_r|}{|V_x|}\right)$.

If the primary goal of the nozzle is conversion from static upstream pressure to jet axial momentum, large velocity angle at the nozzle exit is undesirable because a large fraction of momentum goes in radial direction at large velocity angles. Nozzle geometries that have minimal radial velocity at the nozzle exit can generate a sustainable coherent liquid jet [50]. The liquid jet having a higher fraction of radial velocity have a tendency to produce a more dispersed jet in air [36]. The recent publication shows some evidence of variation in penetration depth in animal skin & gel with respect to jet dispersion angle [59]. It claimed [59] that penetration depth is significantly smaller for turbulent (more dispersed jet) than more focused jet (higher fraction of axial momentum) at same input energy. Liquid jets that have higher axial momentum can therefore be used to deliver drug much deeper into the tissue, whereas jets with relatively higher radial momentum at the nozzle exit may be better suited for drug delivery into dermal tissues.

For all geometries in Fig. 21, we can see that the velocity angle (θ) changes from θ ~ −0.02° near the center of the nozzle exit to θ ~ (−1.2°) to (−3.4°) near the edge of the nozzle exit. Negative sign of a velocity angle suggests that the direction of fluid flow is radially inward. For Richard's function parameters k = −1.5, δ = 0.7, which

(a)

(b)

(c)
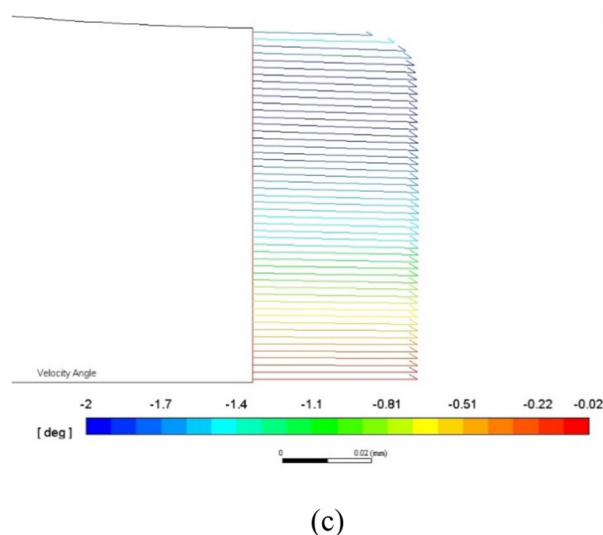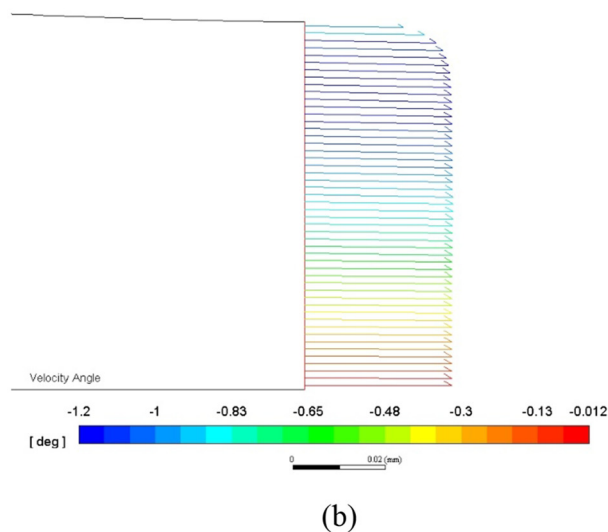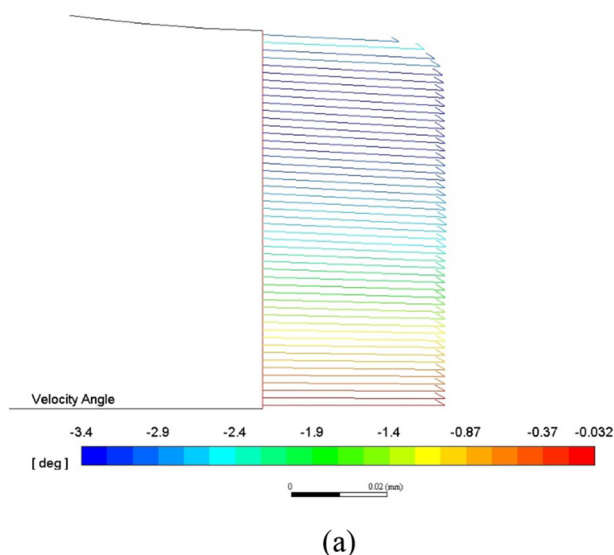
Fig. 21. Velocity vectors at nozzle exit from ANSYS (R18.2) Fluent for Richard's curve parameters: (a) $k = -1.5$, $\delta = 0.7$, (b) $k = -1.5$, $\delta = 0.9$, (c) $k = -2.5$, $\delta = 0.9$. Simulated for water at $\overline{v}_j = 150$ m/s, $d_o = 157.4$ μm (Re = 23,610).
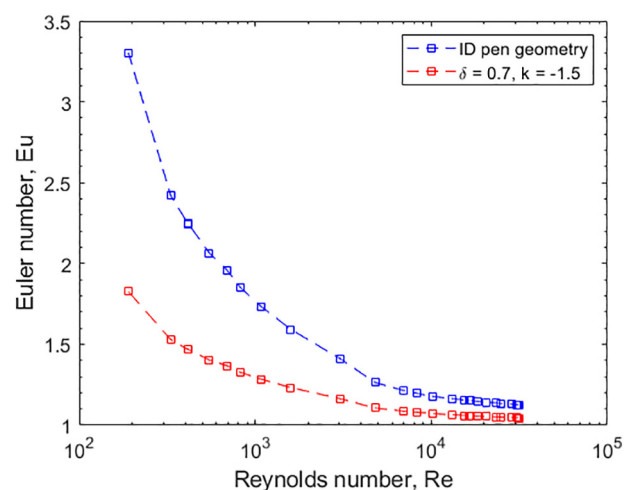
Fig. 22. Euler number versus generalized Reynolds number (Re$_{gen}$) for Carreau fluids. Simulated for all Carreau fluid parameters given in Table 2. $\overline{v}_j = 150$ m/s.

shows minimum pressure losses throughout the range of Reynolds number in Fig. 19, occurrence of maximum radial flow at the nozzle exit is found with the lowest $\theta = -3.4°$ at the nozzle exit. On further analysis, we found that Richard's function geometries with higher nozzle mechanical efficiencies usually possess higher radial momentum at nozzle exit. This suggests that the choice of nozzle geometry from Richard's function can be made by balancing between the nozzle mechanical efficiency and the fraction of radial momentum at the nozzle exit. In case of needle-free jet injectors, this implies that relatively more upstream pressure energy is required to produce a jet with higher axial momentum and possibly deeper tissue injection and vice versa.

From Fig. 22, we found that the Richard's function geometry, which has lowest Euler number over a range of Reynolds number for Newtonian fluids, is also valid for the shear-thinning Carreau fluids over the range of generalized Reynolds number given by Eq. (5). Fig. 22 also shows the characteristic transition from viscous dominant flow to inertia dominant flow, for both the geometries. For all fluids i.e., Newtonian and shear-thinning Carreau fluids, Richard's function has capability to generate nozzle geometries, which have better mechanical efficiencies than conventional conical taper or multi-tier taper. The 'k' and 'δ' parameters in Richard's function to design different nozzle geometries can be selected based upon the fraction of axial momentum required from the liquid jet at the nozzle exit. For spring-powered needle-free jet injectors, this provides an easy way to control the fraction of axial momentum, and therefore potentially penetration depth into the tissue, without changing the setup for the spring or the plunger.

4. Conclusions

We have conducted a combined experimental-numerical study of fluid flow through tapered micro-orifices, with the primary application being needle-free jet injection. The key parameters for our study, which are known to determine jet coherency and stability, were 1) pressure drop, 2) velocity profile at nozzle exit, and 3) boundary layer development. In the numerical simulations, both geometrical and rheological parameters were considered by simulating around 400 different conditions. By using the Euler number, which is a proxy for mechanical energy efficiency, we compared data for both Newtonian and Carreau fluids over a range of Reynolds numbers, showing that Carreau fluids are typically less efficient when using the generalized Reynolds numbers. However, for a fixed low-shear viscosity, shear-thinning effects were shown to provide a considerable advantage over Newtonian fluids in terms of improved efficiency. This could be of high importance for novel nucleic acid-based drugs, which can be both high-viscosity and shear-thinning.

Through variation of cone angle for conical taper geometries over a large range of Reynolds number, we found that the high-shear region near the orifice is the most significant contributing factor in cartridge pressure losses. Both the length of the orifice and the taper geometry were found to significantly impact the development of the boundary layer in this region, and hence impact the overall mechanical efficiency. To circumvent these issues, the use of a generalized logistic function (Richard's curve) can generate a wide range of asymmetric sigmoid contractions, which provide smooth geometrical transitions. Simulations with these geometries showed that optimized nozzle geometries can be achieved for both Newtonian and Carreau fluid via variation of just two parameters in Richard's function.

For spring-powered jet injectors, we hypothesize that sigmoid contractions provide a facile method to vary the fraction of axial momentum, and potentially control the penetration depth into the tissue, without changing the device design or spring type. This is especially promising for intradermal delivery using jet injectors. Ongoing and future studies will incorporate the transient jet start-up phase in addition to more exotic nozzle orifice designs, to further promote jet collimation or dispersion.

Acknowledgement

Appendix A. Supplementary data

Supplementary data to this article can be found online at https://doi.org/10.1016/j.jconrel.2020.01.013.

References

[1] Hingson, R. A. & Hughes, J. G. Clinical studies with jet injection; a new method of drug administration. Curr. Res. Anesth. Analg. 26, 221–30.

[2] G.W. Bruce, Needle-Free Jet Injection Bibliography, Device & Manufacturer Roster, and Patent List, (2004).

[3] J. Baxter, S. Mitragotri, Needle-free liquid jet injections: mechanisms and applications, Expert Rev. Med. Devices 3 (2006) 565–574.

[4] D. Barolet, A. Benohanian, Current trends in needle-free jet injection: an update, Clin. Cosmet. Investig. Dermatol. 11 (2018) 231–238.

[5] A.B. Baker, J.E. Sanders, Fluid mechanics analysis of a spring-loaded jet injector, IEEE Trans. Biomed. Eng. 46 (1999) 235–242.

[6] A. Schoubben, et al., Dynamic behavior of a spring-powered micronozzle needle-free injector, Int. J. Pharm. 491 (2015) 91–98.

[7] N. Inoue, et al., Possibility and effectiveness of drug delivery to skin by needle-free injector, Int. J. Pharm. 391 (2010) 65–72.

[8] D. Wendell, B. Hemond, N.C. Hogan, A. Taberner, I. Hunter, The effect of jet parameters on jet injection, Proceedings of the 28th IEEE EMBS Annual International Conference, 2006, https://doi.org/10.1016/j.jconrel.2018.04.054.

[9] J. Seok, et al., Investigating skin penetration depth and shape following needle-free injection at different pressures: a cadaveric study, Lasers Surg. Med. 48 (2016) 624–628.

[10] R.M.J. Williams, N.C. Hogan, P.M.F. Nielsen, I.W. Hunter, A.J. Taberner, A computational model of a controllable needle-free jet injector, Proc. Annu. Int. Conf. IEEE Eng. Med. Biol. Soc. EMBS (2012) 2052–2055, https://doi.org/10.1109/EMBC.2012.6346362.

[11] E.O. Ogunti, O.R. Popoola, Fluid mechanics analysis of a voice coil needle free jet injector, Adv. Phys. Theor. Appl. 34 (2014) 60–69.

[12] M. Moradiafrapoli, J.O. Marston, High-speed video investigation of jet dynamics from narrow orifices for needle-free injection, Chem. Eng. Res. Des. 117 (2017) 110–121.

[13] S. Mitragotri, Current status and future prospects of needle-free liquid jet injectors, Nat. Rev. Drug Discov. 5 (2006) 543–548.

[14] J. Schramm, S. Mitragotri, Transdermal drug delivery by jet injectors: energetics of jet formation and penetration, Pharm. Res. 19 (2002) 1673–1679.

[15] S. Mitragotri, Immunization without needles, Nat. Rev. Immunol. 5 (2005) 905–916.

[16] S.S.A.A. Hasson, J.K.Z. Al-Busaidi, T.A. Sallam, The past, current and future trends in DNA vaccine immunisations, Asian Pac. J. Trop. Biomed. 5 (2015) 344–353.

[17] M.R. Prausnitz, S. Mitragotri, R. Langer, Current status and future potential of transdermal drug delivery, Nat. Rev. Drug Discov. 3 (2004) 115–124.

[18] S. Resik, et al., Immune responses after fractional doses of inactivated poliovirus vaccine using newly developed intradermal jet injectors, Vaccine 33 (2015) 307–313.

[19] A.M. Römgens, et al., Penetration and delivery characteristics of repetitive microjet injection into the skin, J. Control. Release 234 (2016) 98–103.

[20] J.R. Schramm-Baxter, S. Mitragotri, Investigations of needle-free jet injections, 26th Annu. Int. Conf. IEEE Eng. Med. Biol. Soc, 4 2004, pp. 3543–3546.

[21] S. Mitragotri, Devices for overcoming biological barriers: the use of physical forces to disrupt the barriers, Adv. Drug Deliv. Rev. 65 (2013) 100–103.

[22] Z.U. Rahman, R.B. Kumar, Needle free injection systems, Int. J. Pharm. Sci. Res. 4 (2013) 132–147.

[23] E.E. Kis, G. Winter, J. Myschik, Devices for intradermal vaccination, Vaccine 30 (2012) 523–538.

[24] M.L. Yarmush, A. Golberg, G. Serša, T. Kotnik, D. Miklavčič, Electroporation-based technologies for medicine: principles, applications, and challenges, Annu. Rev. Biomed. Eng. 16 (2014) 295–320.

[25] A. Ravi, D. Sadhna, D. Nagpaal, L. Chawla, Needle free injection technology: a complete insight, Int. J. Pharm. Investig. 5 (2015) 192.

[26] W. Martanto, S.M. Baisch, E.A. Costner, M.R. Prausnitz, M.K. Smith, Fluid dynamics in conically tapered microneedles, AICHE J. 51 (2005) 1599–1607.

[27] Office of Combination Products, Guidance for Industry and FDA Staff: Technical Considerations for Pen, Jet, and Related Injectors Intended for Use with Drugs and Biological Products, (2013).

[28] K. Chen, H. Zhou, An experimental study and model validation of pressure in liquid needle-free injection, Int. J. Phys. Sci. 6 (2011) 1552–1562.

[29] J.C. Stachowiak, T.H. Li, A. Arora, S. Mitragotri, D.A. Fletcher, Dynamic control of needle-free jet injection, J. Control. Release 135 (2009) 104–112.

[30] T.M. Grant, K.D. Stockwell, J.B. Morrison, D.D. Mann, Effect of injection pressure and fluid volume and density on the jet dispersion pattern of needle-free injection devices, Biosyst. Eng. 138 (2015) 59–64.

[31] A. Mohizin, K.E.R. Roy, D. Lee, S.K. Lee, J.K. Kim, Computational fluid dynamics of impinging microjet for a needle-free skin scar treatment system, Comput. Biol. Med. 101 (2018) 61–69.

[32] R. Portaro, H.D. Ng, Experiments and modeling of air-powered needle-free liquid injectors, J. Med. Biol. Eng. 35 (2015) 685–695.

[33] J. Schramm-Baxter, S. Mitragotri, Needle-free jet injections: dependence of jet penetration and dispersion in the skin on jet power, J. Control. Release 97 (2004) 527–535.

[34] D. Zeng, et al., A mathematical model and experimental verification of optimal nozzle diameter in needle-free injection, J. Pharm. Sci. 107 (2018) 1086–1094.

[35] P. Rohilla, et al., Characterization of jets for impulsively-started needle-free jet injectors: influence of fluid properties, J. Drug Deliv. Sci. Technol. 53 (2019) 101167.

[36] A. Umemura, Model for the initiation of atomization in a high-speed laminar liquid jet, J. Fluid Mech. 757 (2014) 665–700.

[37] M.J. Mccarthy, N.A. Molloy, Review of stability of liquid jets and the influence of nozzle design, Chem. Eng. J. 7 (1974) 1–20.

[38] N. Rajaratnam, S.A.H. Rizvi, P.M. Steffler, P.R. Smy, An experimental study of very high velocity circular water jets in air, J. Hydraul. Res. 32 (1994) 461–470.

[39] J. Baxter, S. Mitragotri, Jet-induced skin puncture and its impact on needle-free jet injections: experimental studies and a predictive model, J. Control. Release 106 (2005) 361–373.

[40] V. Yakhot, S.A. Orszag, Renormalization group analysis of turbulence. I. Basic theory, J. Sci. Comput. 1 (1986) 3–51.

[41] V. Yakhot, S.A. Orszag, S. Thangam, T.B. Gatski, C.G. Speziale, Development of turbulence models for shear flows by a double expansion technique, Phys. Fluids A 4 (1992) 1510–1520.

[42] M.T. Ghannam, M.N. Esmail, Rheological properties of carboxymethyl cellulose, J. Appl. Polym. Sci. 64 (1997) 289–301.

[43] A. Benchabane, K. Bekkour, Rheological properties of carboxymethyl cellulose (CMC) solutions, Colloid Polym. Sci. 286 (2008) 1173–1180.

[44] K. Yasuda, A multi-mode viscosity model and its applicability to non-Newtonian fluids, J. Text. Eng. 52 (2006) 171–173.

[45] R.G. Sousa, M.L. Riethmuller, A.M.F.R. Pinto, J.B.L.M. Campos, Flow around individual Taylor bubbles rising in stagnant CMC solutions: PIV measurements, Chem. Eng. Sci. 60 (2005) 1859–1873.

[46] J. Schramm-Baxter, J. Katrencik, S. Mitragotri, Jet injection into polyacrylamide gels: investigation of jet injection mechanics, J. Biomech. 37 (2004) 1181–1188.

[47] F.J. Richards, A flexible growth function for empirical use, J. Exp. Bot. 10 (1959) 290–300.

[48] I.T. Dosunmu, S.N. Shah, Pressure drop predictions for laminar pipe flow of carreau and modified power law fluids, Can. J. Chem. Eng. 93 (2015) 929–934.

[49] E. Ghassemieh, H.K. Versteeg, M. Acar, The effect of nozzle geometry on the flow characteristics of small water jets, Proc. Inst. Mech. Eng. Part C J. Mech. Eng. Sci. 220 (2006) 1739–1753.

[50] C. Theobald, The effect of nozzle design on the stability and performance of turbulent water jets, Fire Saf. J. 4 (1981) 1–13.

[51] A. Begenir, H.V. Tafreshi, B. Pourdeyhimi, Effect of nozzle geometry on Hydroentangling water jets: experimental observations, Text. Res. J. 74 (2004) 178–184.

[52] M.N. Morgan, V. Baines-Jones, On the coherent length of fluid nozzles in grinding, Key Eng. Mater. 404 (2009) 61–67.

[53] M.N. Morgan, et al., Optimisation of fluid application in grinding, CIRP Ann. - Manuf. Technol. 57 (2008) 363–366.

[54] L. Castillo, X. Wang, W.K. George, Separation criterion for turbulent boundary layers via similarity analysis, J. Fluids Eng. Trans. ASME 126 (2004) 297–304.

[55] R.C. Deo, J. Mi, G.J. Nathan, The influence of nozzle-exit geometric profile on

statistical properties of a turbulent plane jet, Exp. Thermal Fluid Sci. (2007), https://doi.org/10.1016/j.expthermflusci.2007.06.004.

[56] N. Anantharamaiah, H.V. Tafreshi, B. Pourdeyhimi, Numerical simulation of the formation of constricted waterjets in hydroentangling nozzles: effects of nozzle geometry, Chem. Eng. Res. Des. 84 (2006) 231–238.

[57] H. Vahedi Tafreshi, B. Pourdeyhimi, Simulating cavitation and hydraulic flip inside hydroentangling nozzles, Text. Res. J. 74 (2004) 359–364.

[58] J.A. Simmons, et al., Characterization of skin blebs from intradermal jet injection: ex-vivo studies, J. Control. Release 307 (2019) 200–210.

[59] A. Kiyama, et al., Visualization of penetration of a high-speed focused microjet into gel and animal skin, J. Vis. 22 (2019) 449–457.